Physics in Medicine & Biology

IPEM Institute of Physics and Engineering in Medicine

PAPER

Energy-modulated x-ray fluorescence and luminescence emissions from therapeutic nanoparticles

J George, L Giannoni and L J Meng[1]

Department of Nuclear, Plasma and Radiological Engineering, The University of Illinois at Urbana-Champaign, 111E Talbot Lab, 104 S Wright St, Urbana, IL 61822, United States of America

[1]Author to whom any correspondence should be addressed.

E-mail: ljmeng@illinois.edu **(L-J Meng)**

Keywords: XFCT, XLCT, X-PDT

RECEIVED
5 August 2018 AQ1

REVISED
22 October 2018

ACCEPTED FOR PUBLICATION
6 November 2018

PUBLISHED AQ2

Abstract

In this study, we have investigated the possibility of modulating x-ray fluorescence (XF) and x-ray luminescence (XL) emissions from therapeutic nanoparticles (NPs) by fine-tuning the energy of incident x-rays from benchtop x-ray sources. We have carried out detailed experimental studies to determine the strength of XF and XL emissions from Y_2O_3:Eu^{3+} and LaF_3:Tb^{3+} NPs being irradiated with x-rays from benchtop x-ray sources operated with different tube-voltages and coupled to various filter configurations. These studies demonstrated that low-energy x-rays with average energy at around 10–15 keV are the most efficient to stimulate XL emission from the Y_2O_3:Eu^{3+} and LaF_3:Tb^{3+} NPs. The efficiency falls quickly when x-ray energies go above or below the optimum energy range. As one would expect, x-rays with average energy just above the corresponding absorption edge of the target metal would be the most efficient in inducing XF emission. In this study, we have also demonstrated that one could fine-tune the incident x-ray energy to modulate the XL and XF emissions, such as (a) selectively inducing either XL or XF emission from the same type of NPs, (b) inducing preferential XL activation of Y_2O_3:Eu^{3+} over LaF_3:Eu^{3+} or controlling the ratio of XL activation of these two types of NPs, and (c) introducing preferential XF emission from one type of NPs over the other. As a potential application, one could optimize the energy-characteristics of the incident x-rays to facilitate multiplexed combinatorial delivery of photodynamic therapy (X-PDT), where different agents could be administrated and then selectively activated in user-defined spatial and temporal patterns to fulfill combinatorial therapeutic effects. The understanding gained through this study could prove critical for enhancing the therapeutic delivery in X-PDT, and for attaining high-quality x-ray fluorescence computed tomography (XFCT) and x-ray luminescence computed tomography (XLCT) images while minimizing the x-ray dose to the sample.

1. Introduction

Recent developments in nanoparticle (NP) technology has shown promise as delivery agents of anti-cancer therapies. Roughly 13 nanomedicines have been clinically approved in every five-year period since the mid-1990s (Bobo *et al* 2016). Even already approved NPs such as Albraxane® has expanded its use from initial indications such as breast cancer into other indications such as non-small-cell lung cancer over the years (Miele *et al* 2009, Von Hoff *et al* 2013). One of the main advantages seen throughout these nanomedicines is the reduction of side effects through localization of the chemotherapeutics (Anselmo and Mitragotri 2016).

Further improvements are being explored as researchers have begun improving the localization of anti-tumor cytotoxic effects by utilizing an external stimulus to activate the anti-tumor properties of these new NPs. Namely, through a process called photodynamic therapy, these nano-sensitizers in conjunction with a conjugated photosensitizer produce cytotoxic reactive singlet oxygen from incoming photons (Agostinis *et al* 2011, Ma *et al* 2014). During the therapeutic delivery process, a collimated external x-ray beam is used to irradiate the target. The metal atoms within the NPs would preferably absorb the x-rays and induce local

therapeutic effect through photosensitization, thermal ablation or other processes. A group from the University of Chicago has seen promising results in using nanoscale metal-organic frameworks in conjunction with photodynamic therapy to inhibit tumor growth in mice (Lu *et al* 2014). A collaborative work, with Hongmin Chen as leading author, demonstrated tumor suppression in mice utilizing x-ray induced photodynamic therapy (X-PDT) in conjunction with $LiGa_5O_8$:Cr NPs (Chen *et al* 2017). Yet despite this promise, NP-based therapies must always address the concern for toxicity and retention. The toxicity of the two of NPs used in this work, LaF_3:Tb^{3+} and Y_2O_3:Eu^{3+}, have been examined, although more studies need to take place. However, initial studies showed, yttrium oxide-based NPs have not demonstrated appreciable toxicity when functionalized with PEGylation in mouse studies while non-functionalized yttrium NPs showed genotoxicity in HEK293 cells even at concentrations of 50 μg ml^{-1} (Cheng *et al* 2011, Selvaraj *et al* 2014). In embryonic zebrafish, lanthanum-based NPs showed no appreciable genotoxicity when administered at doses below 100 μg ml^{-1} (Wang *et al* 2013).

Inorganic X-PDT nanoparticles, by design, emit both x-ray luminescence (XL) and x-ray fluorescence (XF) photons under external x-ray excitation. XL is produced through a scintillation process, in which the x-ray's interaction with the target produces energetic electrons. These electrons cause the downstream production of lower energy electrons, which can interact with the luminescent center of the scintillating material producing metastable excited electronic states. The decay of these states produces optical emissions at a distinct wavelength. In the case of XF emission, the incoming x-ray may remove an inner orbital electron of the target atom through the photoelectric effect. An outer orbital electron fills this vacancy, and the quantized energy difference between these two produces a characteristic x-ray photon. Many groups have explored using XF and XL signals for XFCT and XLCT imaging of specimens in phantoms and mice (Cong *et al* 2011, Bazalova *et al* 2014, Liu *et al* 2014, Groll *et al* 2015). Depending on the imaging geometry used, 3D XFCT and XLCT imaging were demonstrated to be possible (Manohar *et al* 2013, Ren *et al* 2014).

In this study, we have used a newly constructed benchtop X-PDT/XFCT/XLCT system (Fu *et al* 2013, Groll *et al* 2015) to experimentally explore several bench-top x-ray sources and filter configurations to identify the most effective ways to activate XL and XF emissions while minimizing the radiation dose to the sample. We have also studied the possibility of modulating XL and XF emissions by controlling the energy of incident x-rays from bench-top x-ray sources. As we have experimentally demonstrated, by fine-tuning the energy of incident x-rays, one could selectively turn on either XF or XL emission from the same type of NPs. One could also preferentially active the XL emission from one type of NPs (e.g. Y_2O_3:Tb^{3+}) without significantly activating another type of NPs (e.g. LaF_3:Eu^{3+}), or alter the ratio between the levels XL activation of two different types of NPs. Our experimental studies were based exclusively on artificial phantoms.

The results presented in this paper offered useful insights into x-ray irradiation schemes for effective stimulation of XF and XL emission while minimizing the radiation dose to the sample. These understanding is critical for developing dose-efficient XFCT and XLCT imaging strategies. Our experimental results also indicate the possibility of developing future X-PDT techniques with combinatorial delivery and multiplexed activation of different nano-agents to potentially enhance the therapeutic effects. For example, one could consider the delivery of two types of nano-agents, each containing a different nano-phosphor conjugate to adistinct photon-triggered functional nanoparticle. Once the nano-agents are delivered to the target(s), one could use external x-ray beams, tuned to different energy ranges, to selectively stimulate the XL emission from one of the nano-phosphors and therefore trigger a specific therapeutic effect, or to activate both nano-agents at the same time according to user-defined spatial, temporal and functional patterns. We plan to explore these combinatorial therapeutic strategies in our future studies.

2. Materials and methods

2.1. Experimental setup and nanoparticle samples

The experimental setup used in this measurement is shown in figure 1. It is equipped with two x-ray sources. The first one is an Oxford Instrument Apogee-5500 microfocus polychromatic x-ray source with a tungsten anode that can be operated at up to 50 kVp and 1 mA. A pinhole collimator was placed in front of the x-ray source to create a pencil-beam with an effective diameter of 186 μm FWHM beam when reaching the sample. The second one is a monochromatic x-ray source (GeniX-3D by Xenocs) that has a microfocus x-ray source with a Mo target and a Montel mirror to produce a converging x-rays beam. The emerging x-rays are mostly around 17.4 keV Mo K-alpha peak, with a small contaminated from bremsstrahlung x-rays and a small peak around 19.5 keV corresponding to the K-beta x-ray emission. The intensity of the x-ray beam is around 2.5×10^7 photons per second across a 2D Gaussian profile of 146 μm FWHM at the focal plane located ~21 cm from the x-ray source's reference plate.

To measure the XL signal from the NPs, we used an intensified electron-multiplying charge coupled device (I-EMCCD) camera previously developed in our lab (Meng 2006). The I-EMCCD camera consists of an EMCCD, attached to a de-magnifying (DM) tube through a fiber-taper. The DM tube has a 76 mm diameter entrance

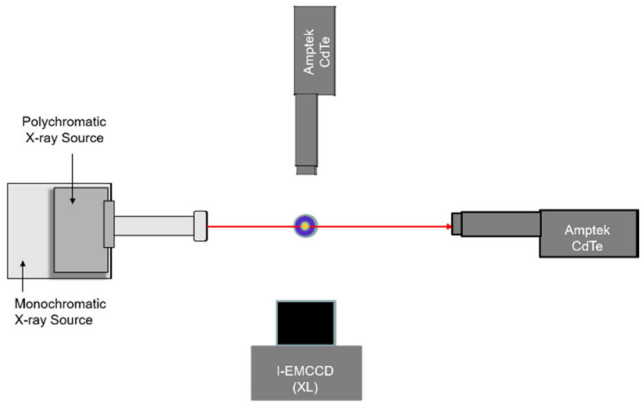

Figure 1. A drawing to demonstrate the setup and geometry. The Amptek XR-100T is placed across the source to gather attenuation information and adjacent to collect XF. Likewise, the I-EMCCD is placed adjacent to collected XL signals. The monochromatic x-ray source is placed on the plane below the polychromatic source, but both sources maintain a 210 mm source to sample distance.

window that receives incident photons and converts the photons into photoelectrons with a red-enhanced bialkali photocathode. The photoelectrons are accelerated through a 10 kV potential-difference and finally impinge onto a thin phosphor applied on the inner surface of the fiber-optic output window to convert the photoelectrons back to visible photons. The DM tube amplifies the number of incident photons by a factor of 10 and spatially condenses the incident photons from its 76 mm entrance window to an output area of around 1.2 cm diameter with a de-magnifying ratio of 6:1. The output of the DM tube is then coupled to the EMCCD camera through a fiber-optic faceplate. The design of the I-EMCCD camera is detailed in Meng (2006).

In this experimental setup, we also included an x-ray camera that has a columnar-grown CsI(Tl) scintillator of 150 μm thickness coupled to a CMOS detector (Andor Zyla, 5.5) to help to position the sample in the beamline. The CMOS camera contains 2560 by 2160 square pixels of 6.5 μm pitch. Additionally, we used two CdTe detectors (Amptek, XR-100T) to detect fluorescence x-rays and to characterize the incident x-ray beam before and after going through the sample. The Amptek XR-100T CdTe detector has a CdTe crystal of 1 mm thickness and 5 mm $\times$ 5 mm active area. The CdTe detector has ~100% photoelectric absorption efficiency for x-rays of the energy of 5 keV to 50 keV (Miele *et al* 2009). The experimental geometry is shown in figure 1.

In this study, we tested two types of nanoparticles, $Y_2O:Eu^{3+}$ and $LaF_3:Tb^{3+}$ in powder form, each placed in a micropipette tip (model number 3120000020, from Eppendorf). A small copper sheet was used to wrap around the tube at around 1.5 cm from the bottom of the pipette to help to position the beam in respect to the region filled with the NPs. A photo of the sample is shown in figure 2.

2.2. Energy selection through x-ray source settings and filtration

With the monochromatic and the polychromatic sources running at different tube-voltages and coupled with various filters, we were able to produce x-ray beams with a variety of energy-spectra. These source configurations are summarized in the following three groups:

Group 1: The polychromatic tube without filtration. In this configuration, no filters are added to the source. Note that there is a Be window that comes with the tube packaging. The x-ray source was operated at its maximum current of 1 mA for all XL and XF studies, and the tube-voltage was varied from 10 kVp to 50 kVp with 5 kVp increments, leading to a total of nine tube-voltages.

Group 2: The polychromatic source with filtration. We used three materials, cerium (K-edge = 40.41 keV), aluminum (K-edge = 1.56 keV) and tungsten (L-edge = 12.92 keV). These were chosen to reduce the spectral spread for the outgoing x-rays around the energies of the K-edges of the two NPs to maximize the probability for photoelectric absorption. The actual filter configurations are detailed as follows:

- 100 μm thickness of Ce,
- 200 μm of Ce,
- 200 μm of Ce and 5 mm of Al,
- 200 μm of Ce and 10 mm of Al,
- 100 μm of W,
- 100 μm of W and 3 mm of Al,
- 100 μm of W and 5 mm of Al.

Figure 2. The pipettes were filled with LaF_3:Tb^{3+} or Y_2O_3:Eu^{3+} NP's.

These filtration schemes allowed us to create relatively narrow energy distributions around 36 keV (with Ce/Al filter) and around 40 keV (with W/Al filter), which were tailored for selective activation of LaF_3:Tb^{3+} nanoparticles. Note that the K-edge of La is at 32 keV. For these measurements, the polychromatic X-ray tube was operated at 50 kVp and 1 mA.

Group 3: A monochromatic x-ray source that generates a converging beam of x-rays with energies peaking at 17.4 keV. As we showed later in figure 5, the outgoing x-rays also have a small peak at 19.5 keV, but its intensity is two orders of magnitude lower than the intensity of the 17.4 keV peak. Therefore these 19.5 keV x-rays would have negligible influence on the quantitative measurements. The 17.4 keV x-rays from the monochromatic x-ray source matches well with the K-absorption-edge at 16.4 keV for yttrium (from Y_2O_3:Eu^{3+} NPs), leading to enhanced photoelectric absorption.

2.3. XF data acquisition and processing

An Amptek XR-100T CdTe detector was used to collect the XF emission from the NPs. The CdTe detector was placed at 5 cm away from the beam line. To remove the contamination from scattered x-rays to the measured XF signal, every individual XF data point was derived from a pair of measurements, one with an empty plastic tube and the other one with an identical tube filled with the NP sample. Both measurements were taken with identical geometry and detector setup. An example of this procedure is shown in figure 3. The top-left plot shows a spectrum of x-rays scattered off the empty tube and reached the detector. The top right plot shows the combined contribution from both XF from the same tube containing NPs and from scattered photons. The bottom plot shows the subtraction of the top two spectra. All counts in the subtracted energy spectrum and within the depicted energy windows, selected for the metals-of-interest, were counted as the fluorescence contribution. Similar procedures were used in several previous studies (Institute 1997, Kuang *et al* 2013, Ding *et al* 2014).

2.4. XL data acquisition and processing

In this study, we used the I-EMCCD detector to collect the XL signal. A suite of codes in MATLAB and C were used for processing the XL data acquired with the I-EMCCD detector. The raw data frames consisting of 512 $\times$ 512 pixels were corrected for dead pixels, pixel-to-pixel variation, shifting pedestal values over time, and hot pixels in the detector assembly. We have developed a data processing code applied to the raw frames acquired in a sequence, which constantly tracks the variation of the pedestal level of each pixel on the EMCCD and subtract the real-time corrected pedestal value from the measured pixel value to derive the true XL signal induced on the pixel. To remove ambient noise contribution, we derived the XL signal by doing two measurements under the identical geometry, one with the x-ray source turned on and the other one with x-ray off, and then subtracting the two sets of signals to obtain the true XL signal.

2.5. Measurement of the x-ray energy attenuated by the sample

We used the Amptek XR-100T CdTe detector placed directly against the beam to measure the energy carried by the incident x-rays and subsequently removed by the sample. For both the monochromatic and the polychromatic x-ray sources, the incident x-ray beams were confined in a pencil beam of less than 200 μm in diameter. The Amptek XR-100T CdTe detector has an active area of 5 mm $\times$ 5 mm. A 2 mm $\times$ 2 mm pinhole collimator was placed in front of the detector to minimize the contribution from scattered photon reaching the detector.

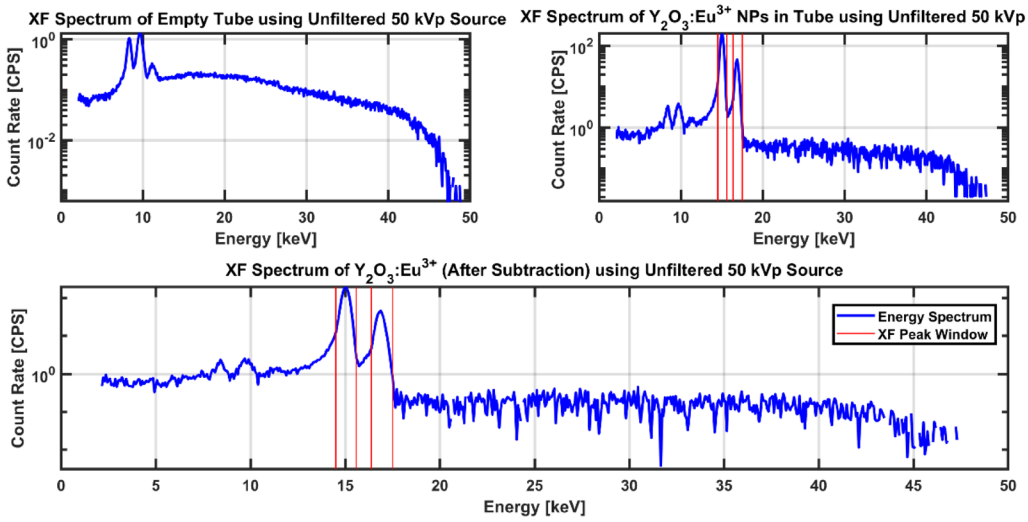

Figure 3. The XF signal was calculated by first obtaining the scattering spectrum from the empty tube (top left) as well as the signal from sample (top right). The scattered spectrum was subtracted from the XF spectrum. Finally, as another means of subtracting the XF fluorescence data the regions above and below the fluorescence peaks are used to calculate a scattering baseline to subtract from the spectrum as well (bottom). Note that all the plots in this figure have a logarithmic scale *y*-axis.

Similar to the measurement of XF signals, we used the CdTe detector to acquire the energy spectra with the x-ray beam passing through three samples, which include an empty micropipette tip and two other identical tips filled with LaF_3:Tb^{3+} and Y_2O:Eu^{3+} samples. By subtracting the measured x-ray spectra with and without the sample in the beam, we could derive the spectrum of x-ray photons that were removed from the beam by the interactions with the sample. An example of this spectral subtraction process is shown in figure 4. By integrating over the subtracted x-ray energy spectrum as also shown in figure 4, we could derive the amount of energy that was originally carried by the incident x-ray beam and subsequently removed from the beam by the interactions with the samples. This integrated total attenuated energy should be equivalent to the amount of energy being transferred to the secondary electrons (i.e. Compton recoil electrons and photoelectrons) through Compton and photoelectric effects. The ratio between the attenuated energy and the mass of the receiving media is typically referred to as the KERMA dose widely used in dosimetry literature. In this study, we used this experimentally derived attenuated energy to normalize the measured XL and XF signals. This allowed us to compare the dose-efficiency of different x-ray irradiation schemes for stimulating XL and XF emission.

3. Results and discussions

3.1. Effects of incident x-ray energy on XL emission

In this study, we have measured the XL and XF signals from the Y_2O_3:Eu^{3+} and (*E*) LaF_3:Tb^{3+} nanoparticles irradiated by x-rays produced with various source and filter configurations, which have their corresponding energy spectra shown in figures 5 and 6. The XL emission from the Y_2O_3:Eu^{3+} and LaF_3:Tb^{3+} NP samples were measured with the I-EMCCD detector using the protocol described in section 2.5.

Figures 7(A) and (B) show the measured XL yields from the Y_2O_3:Eu^{3+} and LaF_3:Tb^{3+} nanoparticles as a function of the rate of energy attenuation by the sample. Figures 7(C) and (D) re-plot the same data as shown in figures 7(A) and (B), but with a different *X*-axis that represents the average energy of the photons being attenuated by the sample. This quantity is referred to as average attenuated photon energy (AAPE), which was derived by averaging over the measured energy spectrum for x-ray photons removed from the beam by the interactions with the sample. In figures 7(E) and (F), we plot the dose-normalized XL yields (XL yields per unit energy attenuated in the sample) as a function of AAPE. These results provided useful insights for optimizing x-ray irradiation scheme for efficient stimulation of XL emission, which is summarized as the following:

- X-rays with energies between 10 and 15 keV appear to be the most efficient for stimulating XL emission from Y_2O_3:Eu^{3+} and LaF_3:Tb^{3+} NPs. These x-rays are able to produce the strongest XL signal per unit energy attenuated in the sample. This statement is supported by the following three sets of measurements. First, when the Y_2O_3:Eu^{3+} NPs were irradiated with the polychromatic x-ray source without extra filter, the efficiency for exciting XL emission initially increases with raising tube-voltage and reaches its maximum at a tube-voltage of 25 kVp, which is corresponding to an AAPE of 12.6 keV. For the LaF_3:Tb^{3+} NPs, similar behavior was observed. The maximum efficiency for stimulating XL emission was achieved with a tube-

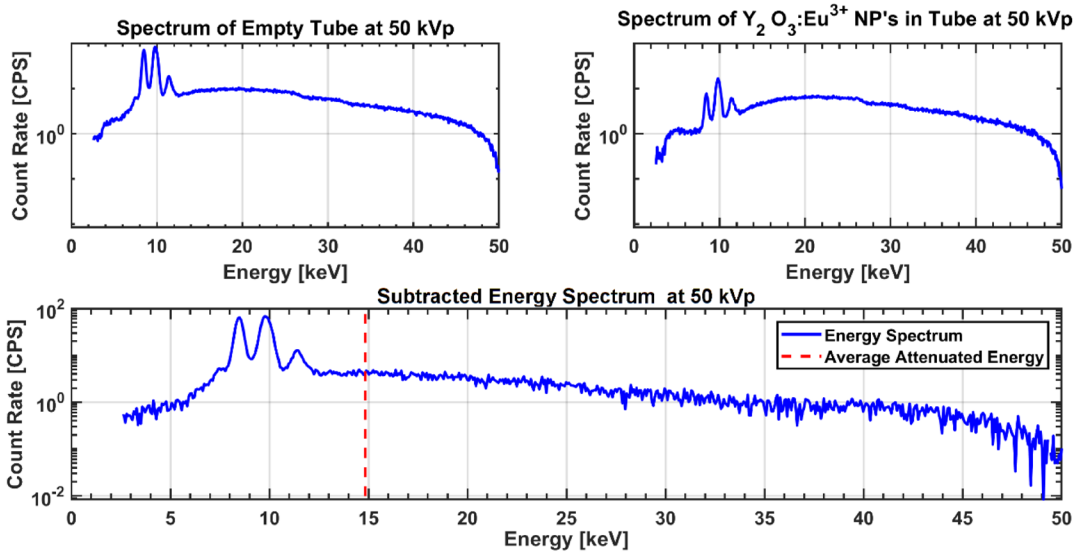

Figure 4. The plot in the top left shows the spectrum (in counts per second) of the empty tube irradiated by the polychromatic source operating at 50 kVp tube-voltage. The plot in the top right shows the spectrum of the Y_2O_3:Eu^{3+} NP's attenuating the beamline. The Yttrium K-edge of 17.02 keV is quite evident in the spectrum. Both spectra displayed account for detector deadtime. The subtracted spectrum of these two spectra is shown in the bottom panel. All three figures have the y-axis in logarithmic scale.

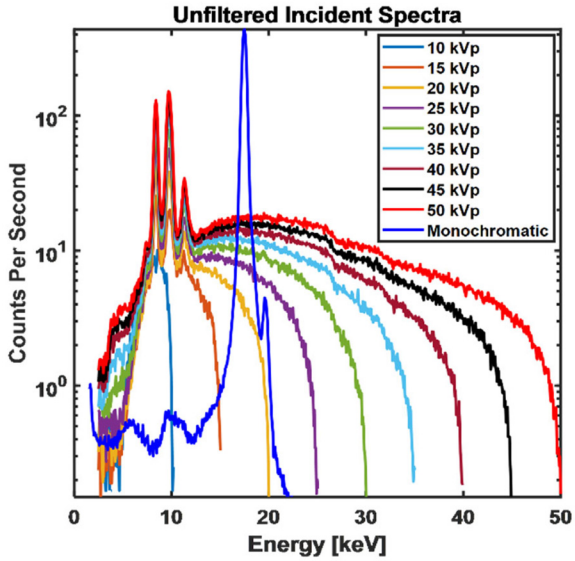

Figure 5. The incident spectrum for the unfiltered polychromatic source at various kVp as well as the monochromatic source. The *y*-axis is the counts per second in logarithmic scale. Both the monochromatic source and polychromatic source were operating at 0.01 mA tube current.

voltage of 30 kVp, leading to an AAPE of 12.4 keV. Beyond these peaking tube-voltages, the efficiency for stimulating XL emission decreases monotonically with increasing tube-voltages. Second, applying filters on the polychromatic source significantly hardened the outgoing x-ray beam, leading to much higher AAPE's as shown in figures 7(C) and (D). These configurations lead to a poor efficiency for stimulating XL emission from the Y_2O_3:Eu^{3+} and LaF_3:Tb^{3+} NPs. *Third*, the 17.4 keV monochromatic x-ray beam has lead to one the lowest dose-efficiencies for stimulating XL emission from Y_2O_3:Eu^{3+} and LaF_3:Tb^{3+} NPs, which is shown in figures 7(E) and (F).

- For both Y_2O_3:Eu^{3+} and LaF_3:Tb^{3+} NPs, the most efficient XL excitation was achieved with incident x-rays that led to AAPE values well below the K-absorption edges of the corresponding metal elements, i.e. yttrium (AAPE: 12.6 keV versus K-edge: 16 keV) and lanthanum (AAPE: 12.4 keV versus K-edge: 38.9 keV). This indicates that photoelectric absorption by L-shell and M-shell electrons has been the predominant effects that led to XL emission. Note that a 12.5 keV x-ray interacts with an L-shell electron (L-edge at 2.37 keV) in a yttrium atom would lead to a photoelectron carrying 12.5–2.37 = 10.13 keV. Similarly, a 12.5 keV x-ray photon absorbed by an L-shell electron in a lanthanum atom (binding energy of 6.2–5.4 keV) would produce

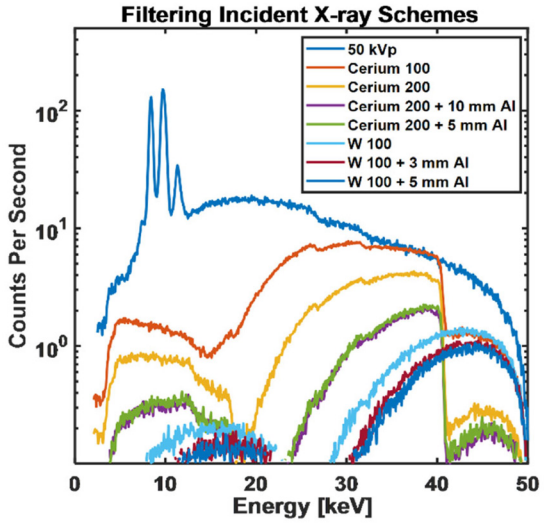

Figure 6. The filtration schemes were performed using the polychromatic source operating at 50 kVp. For acquiring the incident spectra, the x-ray tube was reduced to 0.1 mA to prevent detector saturation. The y-axis is logarithmically scaled counts per second.

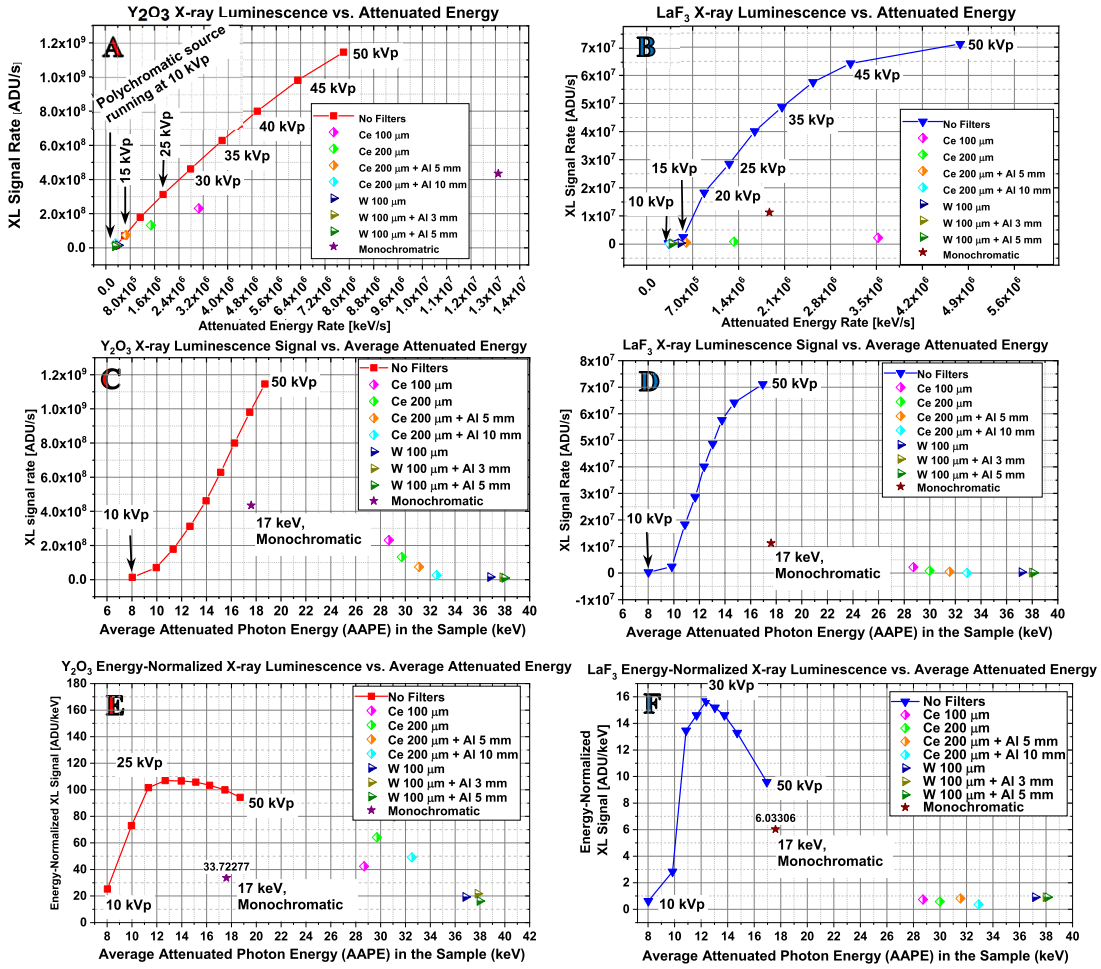

Figure 7. The figures show the XL signal (in ADU) produced for the energy attenuated by the sample per second for various kVP and filtering concentrations for (A) Y_2O_3:Eu^{3+} and (D) LaF_3:Tb^{3+}. Each point is a 5 kVp increment of the polychromatic source from 10 kVp to 50 kVp. The next set of figures show a similar set of information for (B) Y_2O_3:Eu^{3+} and (E) LaF_3:Tb^{3+} but with the X-axis representing the average energy of the photon attenuated by the sample. The last set of figures normalize the ADU by th energy attenuated by the sample per second for (C) Y_2O_3:Eu^{3+} and (F) LaF_3:Tb^3.

a photoelectron of 6.3–7.1 keV. When x-rays excite and liberate electrons, these electrons can liberate other electrons forming a cascade of secondary, tertiary, and so on generations of electrons. Various literature on the subject of XL suggest that light production in nano-phosphors is more dependent on the production of these low energy electrons. These low-energy electrons could then interact with the nano-phosphor and produce excited electron energy states within the nano-phosphor, which will eventually de-excite through the emission of fluorescence and phosphorescence photons, or through other emission-less decay processes (dos Rezende *et al* 2016, Dobrowolska and Zych 2017). Our results presented in figure 7 seem to coincide with these previous observations.

- In order to achieve a dose-efficient XL excitation and subsequently enhance X-PDT effect, one could pair metal-containing nano-agents with selected incident x-ray energies to encourage the creation of secondary electrons at the optimal energy range (5–10 keV). Our experimental results indicated that low-energy x-rays with an average photon energy of 10–15 keV are far more efficient than regular diagnostic x-rays of 60–150 keV and megavoltage x-rays for stimulating XL emission from X-PDT nano-agents currently being experimented for X-PDT treatment.

3.2. Effects of incident x-ray energy on XF emission

Figures 8(A) and (B) show the XF yield as a function of the rate of energy-attenuation in the samples. Figures 8(C) and (D) show the same XF yields as a function of AAPE. Figures 8(E) and (F) plot the dose-normalized XF yields, defined as XF signal amplitude per unit energy attenuated in the sample, as a function of AAPE. The monochromatic source is not used in this study. The 17.4 keV photon energy is significantly lower than the 38.89 keV K-edge of Lanthanum, and thus would not produce K-X-ray fluorescence signal.

There have been a vast number of synchrotron and non-synchrotron based XF experiments that were conducted with optimized x-ray energy according to the absorption edge of the target metal (Boisseau and Grodzins, Lobinski *et al* 2006, Jones *et al* 2012, Fu *et al* 2013, Davies *et al* 2014, Bazalova-Carter *et al* 2015). In our study, the monochromatic (17.4 keV) x-ray source was the most efficient in stimulating K-X-ray fluorescence emission from the Y_2O_3:Eu^3 NPs (yttrium K-edge is at 15.9 keV). However, one could achieve a similar efficiency by using a regular polychromatic x-ray source with a simple filter. For example, adding a cerium filter of 100 μm thickness to the polychromatic source running at 50 kVp effectively reduces the flux of lower energy photons (shown in figure 6), leading to an AAPE of 26 keV. This configuration gave the second-best dose-efficiency for stimulating XF emissions from the Y_2O_3:Eu^{3+} nanoparticles. By comparison, the same polychromatic source running at a tube-voltage of 40 kVp and without filtering would lead to an AAPE of 16 keV, which also offered a reasonable dose-efficiency for stimulating XF emission. These results are shown in figure 8(E).

For the LaF_3:Tb^{3+} NPs, the most efficient XF excitation was achieved by running the polychromatic x-ray source at 50 kVp and filtering the out-going x-rays with a tungsten filter of 100 μm thickness, followed by an aluminum filter of 3 mm thickness. This configuration led to an AAPE of 38 keV, which is close to the 38.89 keV Lanthanum K-edge.

3.3. Selective excitation of XL and XF emissions

We have further explored the possibility of using x-ray beams of different average energies to selectively activate either XF or XL emissions from different types of nanoparticles. Figures 9(A) and (B) shows the ratio between XL/XF yields from Y_2O:Eu^{3+} and LaF_3:Tb^{3+} NPs as a function of AAPE. In figure 9(C), we plot the ratio between the energy-normalized XL yields from Y_2O:Eu^{3+} and LaF_3:Tb^{3+} also as a function of AAPE.

The polychromatic x-ray source running at 10 kVp could effectively activate the XL emission from Y_2O:Eu^{3+} NPs, but the same x-ray beam could only weakly activate the XL emission from LaF_3:Tb^{3+}. If we tune up the tube-voltage from 10 kVp to 20 kVp, the activation of XL signal from LaF_3:Tb^{3+} increased monotonically, while the XL signal from Y_2O:Eu^{3+} NPs initially increased and peaked at 15 kVp, then falls quickly with increasing tube-voltage. As a result, the ratio of the XL emission from Y_2O:Eu^{3+}/LaF_3:Tb^{3+} XL changed dramatically from 42 to 7. This result indicates that one could use a benchtop x-ray generator to selectively activate one type of NPs without significant activation of the other type, or to control the relative levels of XL activation for two types of NPs.

Finally, we plotted the ratio between the energy-normalized XF yields from Y_2O:Eu^{3+} and LaF_3:Tb^{3+} against AAPE in figure 9(D). Similar to the results shown in figure 9(C), one could also selectively active XF emissions from a given type of NPs without significant activation of the XF emission from the other type, even though both types of nanoparticles are co-localized in the same region being irradiated by the same x-ray beam. Several remarks regarding these experiential results are summarized below:

- *Selective excitation between XF and XL emissions*. Since XL emission favors stimulations with lower-energy x-rays, and XF emission favors higher energy x-rays, one could consider an image-guided X-PDT delivery strategy, in which one would use lower-energy x-rays to activate the x-PDT effect with a maximum

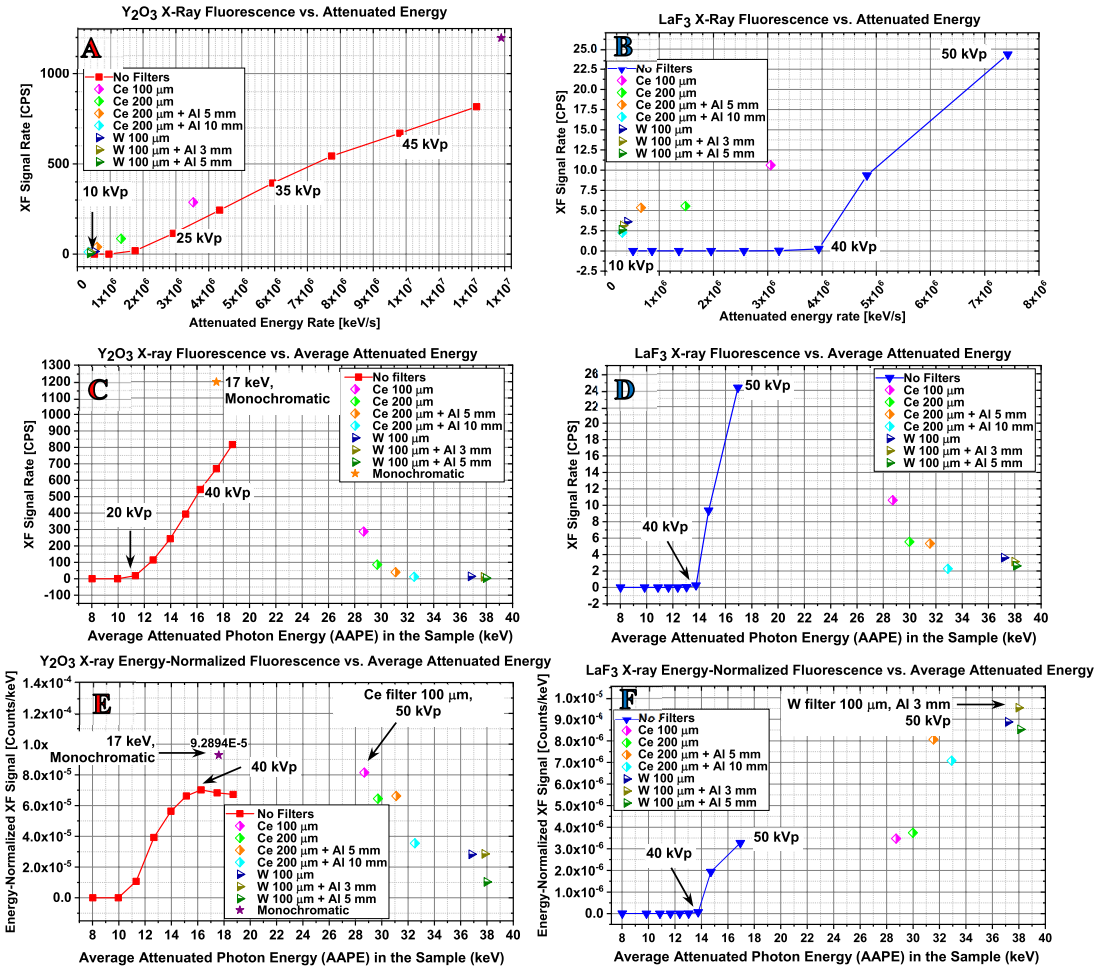

Figure 8. The figures show XF counts produce for the energy attenuated by the sample per second for various kVP and filtering concentrations for (A) Y_2O_3:Eu^{3+} and (D) LaF_3:Tb^{3+}. Each point is a 5 kVp increment of the polychromatic source from 10 kVpt to 50 kVp. The next set of figures show a similar set of information for (B) Y_2O_3:Eu^{3+} and (E) LaF_3:Tb^{3+} but with the *X*-axis representing the average energy of the photon attenuated by the sample. The last set of figures normalize the counts by the energy attenuated by the sample per second for (C) Y_2O_3:Eu^{3+} and (F) LaF_3:Tb^3.

dose-efficiency, and then switch to higher energy x-rays to stimulate XF emission for mapping the target NPs. As shown in figure 9(A), the use of the polychromatic x-ray source running at 15 kVp (with a corresponding AAPE of 9.8 keV) could effectively activate XL emission from Y_2O_3:Eu^{3+} NPs, but could not activate XF emission from the same NP. Increasing the tube-voltage to 25 kVp (AAPE: 12.7 keV), the level of XL emission is suppressed, but the level of XF emission reaches its maximum, so the ratio between XL and XF emissions falls to near minimum. The monochromatic x-ray source with its 17.4 keV energy was very efficient in stimulating XF emission from yttrium but was inefficient to stimulate XL emission, and therefore minimizes the ratio between XL and XF emission from Y_2O_3:Eu^{3+} NPs.

- *Selective activation of XL emission from different nano-phosphors.* In figure 9(C), we have demonstrated that one could use the lower-energy x-rays from the polychromatic source running at 10 kVp (AAPE: 8 keV) to selectively activate Y_2O_3:Eu^{3+}, while keeping the activation of LaF_3:Tb^{3+} to a minimum. By raising the tube-voltage of the polychromatic x-ray source from 10 kVp to 20 kVp (with the corresponding AAPE values changing from 8 keV to 12 keV), one could change the ratio between XL yields from Y_2O_3:Eu^{3+} and LaF_3:Tb^{3+} by a factor of 6 (from 42 to 7).
- *Selectively activation of XF emission from nanoparticles containing different metal elements.* As we showed in figure 9(D), running the polychromatic tube at 30 kVp would maximize XF yield from Y_2O_3:Eu^{3+} without the activation of the XF emission from LaF_3:Tb^{3+}. The monochromatic (17.4 keV) x-ray source would be the most effective in producing XF signal from Y_2O_3:Eu^{3+} and no lanthanum XF would be produced. Pushing the tube-voltage from 30 keV to 50 keV would reduce the XF emission from Y_2O_3:Eu^{3+} NPs, while improving the XF emission from LaF_3:Tb^{3+} by a factor of 30.

In this study, we have used x-rays of less than 50 keV to stimulate XL and XF emission from two types of nanoparticles, Y_2O_3:Eu^{3+} and LaF_3:Tb^{3+}, each containing a heavy metal element. Under these experimental settings,

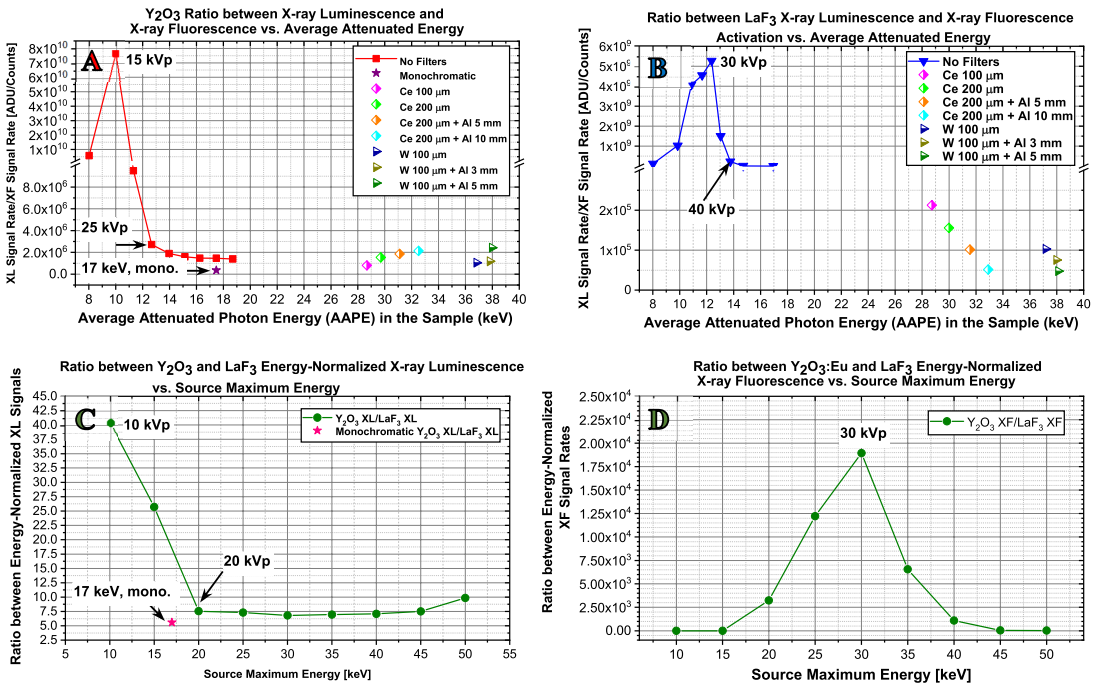

Figure 9. The figure depicts different means of activating XL over XF ratio for (A) Y_2O_3:Eu^{3+} and (B) LaF_3:Tb^{3+}. (C) depicts the ratio between XL signals of Y_2O_3:Eu^{3+} and LaF_3:Tb^{3+} for various maximum source energies while (D) depicts the XF equivalent.

the interactions between the incoming x-rays and the nanoparticles are primarily photoelectric absorption. The strength of XL and XF emission would critically depend on how the energy spectrum of incident x-rays matches the photoelectric cross-section of the target metal, especially the abrupt change in photoelectric cross-session around the K-, L- and M-absorption edges. This allowed us to use x-ray beams of different energies to selectively stimulate the XF emission from different nanoparticles.

We have also demonstrated that the XL emission from the Y_2O_3:Eu^{3+} and LaF_3:Tb^{3+} nanoparticles are mostly originated from the energy absorbed through photoelectric interactions of low-energy (10–15 keV) x-rays with L-shell and M-shell electrons of the target metal atoms. It is therefore possible to exploit the differences in the photoelectric cross-sections as functions of x-ray energy for different metals to allow selective activation of XL emission from one type of nanoparticles without activating other types, or to control the relative levels of XL activation of different types of nanoparticles co-existing in the target.

4. Conclusions

In this study, we have experimentally explored the possibility of using x-rays of different energies to modulate XF and XL emissions from therapeutic nanoparticles. We have demonstrated that low-energy x-rays of 10–15 keV would be the most effective in inducing XL emissions from Y_2O_3:Eu^{3+} and LaF_3:Tb^{3+} nanoparticles and higher-energy x-rays with an average attenuated photon energy of similar to or slightly higher than the corresponding (K- or L-) absorption-edge of the target metal would be the most effective in stimulating XF emissions.

Furthermore, one could selectively activate the XL or XF emission from one type of nano-particles without significant activation of the other type(s), or control the relative strengths of XL or XF emissions from two (or more) different types of NP's coexisting within the same sample. These results demonstrated the possibility for multiplexed activation of different nano-agents within the same target and combinatorial delivery of X-PDT effects.

From instrumentation viewpoint, while our choice of the specific 50 kVp x-ray source with a Mo target is a compromise based on what we currently have at hand, the results shown in this paper demonstrated that one could construct a combined XFCT, XLCT and X-PDT system based a single x-ray source that is capable of delivering x-ray photons of a sufficiently high energy for XF imaging, while offering the option of using lowered tube-voltage and filtration to produce lower-energy x-rays for XL excitation and the activation of X-PDT effect.

We have so far demonstrated these possibilities with Y_2O_3:Eu^{3+} and LaF_3:Tb^{3+} NPs, but there would be a wide variety of different NPs that could be considered for this multiplexed activation scheme. The understanding of how to effectively activate the XL emission with external x-ray irradiations could help the design of an appropriate combination of nano-agents and sources to fulfill this potential.

AQ4 AQ3

References

Agostinis P *et al* 2011 Photodynamic therapy of cancer: an update *CA Cancer J. Clin.* **61** 250–81

Anselmo A C and Mitragotri S 2016 Nanoparticles in the clinic *Bioeng. Transl. Med.* **1** 10–29

AQ5 Bazalova M, Ahmad M, Pratx G and Xing L 2014 L-shell x-ray fluorescence computed tomography (XFCT) imaging of Cisplatin *Phys. Med. Biol.* **59** 219–32

Bazalova-Carter M, Ahmad M, Xing L and Fahrig R 2015 Experimental validation of L-shell x-ray fluorescence computed tomography imaging: phantom study *J. Med. Imaging* **2** 043501

Bobo D, Robinson K J, Islam J, Thurecht K J and Corrie S R 2016 Nanoparticle-based medicines: a review of FDA-approved materials and clinical trials to date *Pharm. Res.* **33** 2373–87

Boisseau P and Grodzins L 0000 Fluorescence tomography using synchrotron radiation at the NSLS *Hyperfine Interact.* **33** 282–92 AQ6

Chen X S H, Wang G D, Nagata K, Hao Z, Wang A, Li Z, Xie J and Shen B 2017 $LiGa_5O_8$:Cr-based theranostic nanoparticles for imaging-guided x-ray induced photodynamic therapy of deep-seated tumors *Mater. Horiz.* 1092–101 AQ7

Cheng L, Yang K, Shao M, Lu X and Liu Z 2011 *In vivo* pharmacokinetics, long-term biodistribution and toxicology study of functionalized AQ8 upconversion nanoparticles in mice **6** 1327–40

Cong W, Shen H and Wang G 2011 Spectrally resolving and scattering-compensated x-ray luminescence/fluorescence computed tomography *J. Biomed. Opt.* **16** 066014

Davies K M *et al* 2014 Copper pathology in vulnerable brain regions in Parkinson's disease *Neurobiol. Aging* **35** 858–66

Ding H, Cho H M, Barber W C, Iwanczyk J S and Molloi S 2014 Characterization of energy response for photon-counting detectors using x-ray fluorescence *Med. Phys.* **41** 121902

Dobrowolska A and Zych E 2017 The mechanism of x-ray excited luminescence in $BaHfO_3$ doped with Eu^{3+}, Y^{3+} or Eu^{3+}, La^{3+} *J. Lumin.* **192** 397–403

dos Rezende M V S, Andrade A B, Macedo Z S and Valerio M E G 2016 Mechanism of x-ray excited optical luminescence (XEOL) in Eu-doped $BaAl_2O_4$ nanopowders *Phys. Chem. Chem. Phys.* **392** 44–9

Fu G, Meng L J, Eng P, Newville M, Vargas P and La Riviere P 2013 Experimental demonstration of novel imaging geometries for x-ray fluorescence computed tomography *Med. Phys.* **40** 061903

Groll A, George J, Vargas P, La Riviere P J and Meng L J 2015 Element mapping in organic samples utilizing a benchtop x-ray fluorescence emission tomography (XFET) system *IEEE Trans. Nucl. Sci.* **62** 2310–7

International Atomic Energy Agency 1997 Sampling, storage and sample preparation procedures for X ray fluorescence analysis of AQ9 environmental materials **28**

Jones B L, Manohar N, Reynoso F, Karellas A and Cho S H 2012 Experimental demonstration of benchtop x-ray fluorescence computed tomography (XFCT) of gold nanoparticle-loaded objects using lead- and tin-filtered polychromatic cone-beams *Phys. Med. Biol.* **57** N457–67

Kuang Y, Pratx G, Bazalova M, Meng B W, Qian J G and Xing L 2013 First demonstration of multiplexed x-ray fluorescence computed tomography (XFCT) imaging *IEEE Trans. Med. Imaging* **32** 262–7

Liu X, Liao Q and Wang H 2014 Fast x-ray luminescence computed tomography imaging *IEEE Trans. Biomed. Eng.* **61** 1621–7

Lobinski R, Moulin C and Ortega R 2006 Imaging and speciation of trace elements in biological environment *Biochimie* **88** 1591–604

Lu K, He C and Lin W 2014 Nanoscale metal-organic framework for highly effective photodynamic therapy of resistant head and neck cancer *J. Am. Chem. Soc.* **136** 16712–5

Ma L, Zou X and Chen W 2014 A new x-ray activated nanoparticle photosensitizer for cancer treatment *J. Biomed. Nanotechnol.* **10** 1501–8

Manohar N, Reynoso F J and Cho S H 2013 Experimental demonstration of direct L-shell x-ray fluorescence imaging of gold nanoparticles using a benchtop x-ray source *Med. Phys.* **40** 080702

Meng L J 2006 An intensified EMCCD camera for low energy gamma ray imaging applications *IEEE Trans. Nucl. Sci.* **53** 2376–84

Miele E, Spinelli G P, Miele E, Tomao F and Tomao S 2009 Albumin-bound formulation of paclitaxel (Abraxane ABI-007) in the treatment of breast cancer *Int. J. Nanomed.* **4** 99–105

Ren L, Wu D, Li Y, Wang G, Wu X and Liu H 2014 Three-dimensional x-ray fluorescence mapping of a gold nanoparticle-loaded phantom *Radiat. Imaging Phys.* **41** 031902

Selvaraj V *et al* 2014 Cytotoxicity and genotoxicity caused by yttrium oxide nanoparticles in HEK293 cells *Int. J. Nanomed.* **9** 1379–91

Von Hoff D D *et al* 2013 Increased survival in pancreatic cancer with nab-paclitaxel plus gemcitabine *New Engl. J. Med.* **369** 1691–703

Wang K *et al* 2013 Toxicity assessments of near-infrared upconversion luminescent LaF_3:Yb,Er in early development of zebrafish embryos *Theranostics* **3** 258–66